A unifying scaling for the Bauschinger effect in highly confined thin films: a discrete dislocation plasticity study

S. Waheed[a], R. Hao[b], A. Bhowmik[b], D. S. Balint[a,*], F. Giuliani[a,b]

[a] *Department of Mechanical Engineering, Imperial College London, London SW7 2AZ, UK*
[b] *Department of Materials, Imperial College London, London SW7 2AZ, UK*

Abstract

In this study, sequential sputter deposition, diffusion bonding and focused ion beam milling are used to fabricate sapphire micropillars encapsulating a thin single crystal niobium film. A distinct Bauschinger effect is observed during the cyclic axial compression of the samples. Plain strain discrete dislocation plasticity is used to interpret the experimental results obtained for the encapsulated film-micropillar geometry. The simulations show that the experimental samples correspond to a saturated source density regime, producing the maximum Bauschinger effect for the chosen mean nucleation strength. Next, the source density and mean nucleation strength are shown to have a coupled effect on the size of the Bauschinger effect, understood in terms of the differing number of pile-ups occurring per source in the film. The coupled effect is found to be represented by the density of dislocations annihilated upon unloading: a consistent linear relationship is observed between the size of the Bauschinger effect and the annihilated dislocation density over the entire source density and nucleation strength parameter space investigated. It is found that different film orientations fulfil the same linear relationship, whereas changing the film thickness causes the slope of the linear trend to vary suggesting a length-scale dependence on reverse plasticity. Finally, all results are found to be unified by a power-law relationship quantifying the Bauschinger effect of the form $\Gamma_B \propto \Delta\rho_{ann} l^n$ where it is argued that the number of dislocations undergoing reverse glide in the confined film is represented by $\Delta\rho_{ann}$, the mean free path of dislocations by l and the effect of hardening processes by the exponent n. The net reverse glide is thus represented by $\Delta\rho_{ann} l^n$ which can be used as a measure of the Bauschinger effect.

Keywords: Discrete dislocation plasticity; Bauschinger effect; thin films; niobium.

1. Introduction

Thin, confined metal layers occur naturally in polycrystalline materials and in nano- and micro-electro mechanical systems (NEMS/MEMS). It is now well established that the mechanical properties of samples at the micro and smaller scales demonstrate a size dependent response which is different from the bulk material [1]. In addition to a size dependent flow stress and hardening rate which have been studied extensively, confined small scale samples demonstrate a significantly stronger Bauschinger effect, the early onset of yielding on reverse deformation, than bulk materials [2]. Understanding the Bauschinger effect is essential for developing accurate plasticity theories and ensuring mechanical integrity of small-scale devices that undergo cyclic straining.

*Corresponding author.
Email address: d.balint@imperial.ac.uk (D. S. Balint)

Confined small-scale systems have been investigated experimentally using the thermomechanical wafer curvature technique [3], plane-strain bulge technique [4], microtensile techniques [5] and passivated micropillars [6]; a distinct Bauschinger effect was observed in these experimental studies. Xiang and Vlassak (2006) [4] observed that for polycrystalline thin films, the size of the Bauschinger effect increases with pre-strain and the number of passivated thin film boundaries. Nicola et al. (2006) [7] used plane strain discrete dislocation (DD) simulations to simulate the experimental results and showed that dislocation pile-ups occurred at the impenetrable interfaces, leading to back stresses that cause reverse dislocation glide upon unloading. This hypotheses was further supported by experimental evidence from Rajagopalan et al. (2008) [8], discrete dislocation simulations in two dimensions by Shishvan et al. (2010) [9], and in three dimensions by Zhou and LeSar (2012) [10] that showed that even unpassivated, polycrystalline thin films demonstrate plastic hysteresis due to reverse dislocation glide from pile-ups at grain boundaries. Guruprasad et al. (2008) [11] found that the extent of reverse plasticity is significantly dependent on the initial source density in discrete dislocation simulations; however, the exact transition with increasing source density was not investigated. Lastly, Jennings et al. (2012) [6] have also observed the existence of the Bauschinger effect in single crystal micropillars passivated with a ceramic coating. Three dimensional DD simulations [12, 13] have shown this to be caused again by dislocation pile-ups at the passivation interface similar to the case for two dimensions.

In order to identify a physically based parameter that can be used for the interpretation and understanding of reverse plasticity, Shishvan et al. (2010) [9] suggested the use of the ratio of free surface to grain boundary area as a measure to classify the Bauschinger effect in unpassivated thin films. However, the effect of pre-strain and number of grain layers was defined separately, not as a combined measure. Despite the significant interest in the Bauschinger effect in small-scale samples, there is yet to be a unifying parameter identified to predict the dependence of the Bauschinger effect on different pre-strains, states of passivation, grain aspect ratios and other geometric effects.

Recently, a new technique for studying confined thin film systems has been developed by Mu et al. (2014) [14]. The technique involves encapsulating a thin metal film within a ceramic micropillar and using micropillar compression to induce plasticity in the thin film. Here, we present new experimental results for the Bauschinger effect observed in thin films using this technique with accompanying plane strain discrete dislocation results to interpret the data. In particular, the emphasis is on understanding the response of the entire specimen comprising the plastic thin film and elastic encapsulation since such coupled systems often exist in NEMS/MEMS devices. The effects of source density, mean nucleation strength, plastic prestrain, film orientation and film thickness on reverse plasticity are investigated in detail. A unifying parameter grouping consisting of the density of dislocations annihilated upon unloading and the mean free path for dislocations is presented as a measure for the amount of net reverse glide and found to represent the size of the Bauschinger effect for all samples considered in this study.

2. Experimental details

Thin niobium (Nb) layers were sputter deposited onto single crystalline sapphire (Al_2O_3) substrates (purity $> 99.99\%$) using magnetron sputtering at room temperature with an Ar gas pressure of $< 10^{-5}$ Torr and 500 mA deposition current in the chamber. Samples were then diffusion bonded at a temperature of 1600 °C with a bonding time of 6 hrs in a hot press furnace, under a pressure of 30 MPa and in a vacuum of less than 10^{-5} Torr. 5 mm $\times$1 mm $\times$1 mm pieces with Nb films encapsulated within sapphire substrates at 45 $^\circ$ incline were prepared by manual polishing. Cylindrical pillars bearing these 45 $^\circ$ Nb interlayers were prepared by focussed ion beam (FIB) milling in a dual beam Helios 600 Nanolab scanning electron microscope (SEM).

The pillars were milled down at a final polishing current of 50 pA. Experimental samples were prepared such that the activated slip systems in the Nb film can be modelled by planar discrete dislocation plasticity with relative crystal orientations being $Nb(111)||Al_2O_3(0001)$. The experimental data presented herein is for a Nb interlayer of 0.3 μm thickness at 45° to the pillar axis and a micropillar height of 9.0 μm and diameter 2.5 μm. The top surface is compressed at a displacement rate of $5 \times 10^{-3}\,\mu m\,s^{-1}$ ($\sim \dot{\varepsilon} = 5 \times 10^{-4}\,s^{-1}$). A representative as-prepared sample is shown in Fig. 1 with a larger film thickness than 0.3 μm to show the Nb layer more clearly.

3. Model

A conventional planar discrete dislocation plasticity (DDP) model was used to simulate the experimental set-up and loading, following the formulation of Van der Giessen and Needleman (1995) [15] and the superposition principle of Lubarda et al. (1993) [16]. Edge dislocations are modelled as infinite straight line defects in an isotropic, linear-elastic medium and plasticity arises from the motion of a large number of these discrete edge dislocations on defined slip planes. The deformation state of the body is calculated in an incremental manner. At each increment, applying linear superposition, the state of the body is decomposed into a dislocation based field ($\tilde{}$) and an image field ($\hat{}$) which corrects for the applied boundary conditions as follows:

$$\mathbf{u}^{DD} = \tilde{\mathbf{u}} + \hat{\mathbf{u}}\,,\ \boldsymbol{\varepsilon}^{DD} = \tilde{\boldsymbol{\varepsilon}} + \hat{\boldsymbol{\varepsilon}}\,,\ \boldsymbol{\sigma}^{DD} = \tilde{\boldsymbol{\sigma}} + \hat{\boldsymbol{\sigma}} \tag{1}$$

where $\mathbf{u}$, $\boldsymbol{\varepsilon}$ and $\boldsymbol{\sigma}$ are the displacement, strain and stress fields respectively. The ($\tilde{}$) field comprises of the sum of all the individual singular, analytical edge dislocation fields in a homogeneous infinite medium [17]:

$$\tilde{\mathbf{u}} = \sum_{i=1}^{N} \tilde{\mathbf{u}}^i\,,\ \tilde{\boldsymbol{\varepsilon}} = \sum_{i=1}^{N} \tilde{\boldsymbol{\varepsilon}}^i\,,\ \tilde{\boldsymbol{\sigma}} = \sum_{i=1}^{N} \tilde{\boldsymbol{\sigma}}^i \tag{2}$$

where N is the total number of dislocations. The ($\hat{}$) field is then superposed to give the correct overall boundary conditions and is determined using the finite element method. Further details of the standard DDP formulation can be found in Van der Giessen and Needleman (1995) [15].

3.1. O'Day method

The analytical dislocation fields forming the ($\tilde{}$) solution are for a homogeneous infinite medium. In the original formulation, the presence of heterogeneities can be accounted for by calculating a polarisation stress [15]; however, this can become computationally expensive when a large number of dislocations and/or inclusions are involved. Instead, an extension of the initial superposition principle proposed by O'Day and Curtin (2004) [18] and later used by Shishvan et al. (2011) [19] can be used to account for different material elastic properties. The method is outlined in [18, 19] but will be explained here briefly, using the terminology employed by Shishvan et al. Each region with different elastic properties is defined as a separate discrete dislocation (DD) subproblem with generic boundary conditions. A complete elastic finite element (FE) subproblem for the entire domain is then superposed to account for the real boundary conditions. The DD subproblems are solved using the conventional DD method outlined above and the elastic subproblem is solved using the finite element method. Linearity implies that the complete solution can be given as the sum of all the DD-subproblems and the FE subproblem. Thus for the displacement variable:

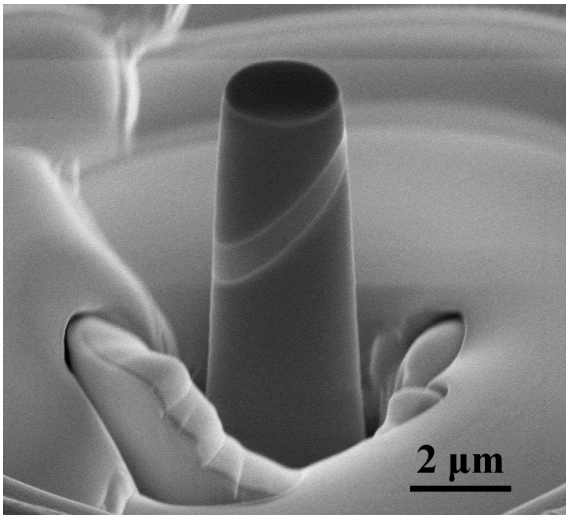


Figure 1: A representative as-prepared experimental sample. A niobium interlayer is encapsulated within sapphire substrates.

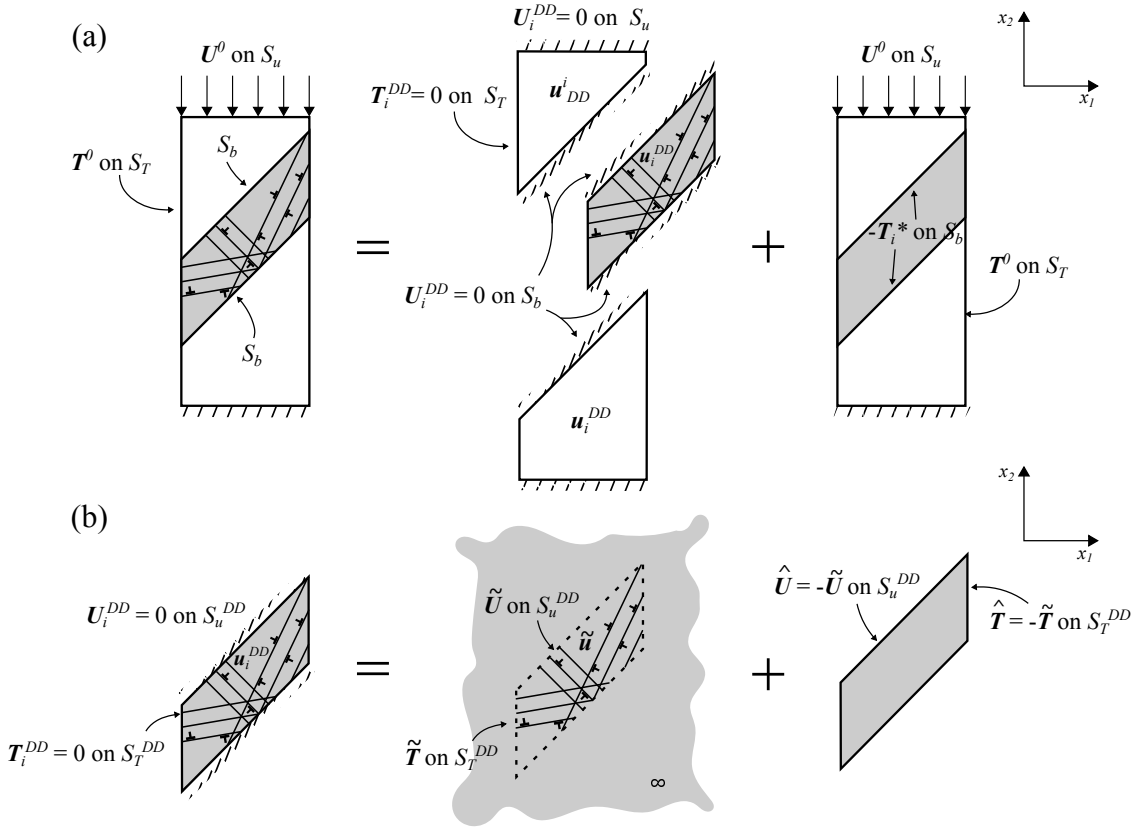


Figure 2: Schematics of the O'Day implementation as applied to the encapsulated film-micropillar geometry. (a) The complete problem is divided into individual DD subproblems and an elastic FE subproblem. (b) The DD subproblems are then solved using a conventional planar DD framework. Note that only the interlayer is allowed to have dislocations in this micropillar problem since the sapphire is considered to be elastic under the loads and temperatures considered here. Therefore, only the interlayer DD subproblem needs to be considered in the O'Day scheme.

$$\mathbf{u} = \sum_{i=1}^{M} \mathbf{u}_i^{DD} + \mathbf{u}^{FE} \tag{3}$$

and similarly for strain and stress, where M is the total number of DD subproblems. Fig. 2 shows the O'Day implementation being applied to the encapsulated-film micropillar geometry with plane strain conditions in the $x_1 - x_2$ plane. For the entire domain, consider displacements $\mathbf{U}^0$ applied to the boundary S_u, tractions $\mathbf{T}^0$ applied to S_T and the boundary between the DD subproblems being S_b. The decomposition of the entire specimen into the DD subproblems and the FE subproblem is shown in Fig. 2(a). The generic boundary conditions applied to the DD subproblems are then chosen as $\mathbf{U}_i^{DD} = 0$ for S_u and S_b and tractions as $\mathbf{T}_i^{DD} = 0$ for S_T as also shown on the figure. The individual DD sub-problems can be solved using the standard DD framework as a superposition of the ($\tilde{}$) and ($\hat{}$) fields for that region as shown in Fig. 2 (b). From each DD subproblem, a traction $\mathbf{T}_i^*$ is obtained along the corresponding S_b. This traction is then input into the FE subproblem as $-\mathbf{T}_i^*$ on S_b and represents the corrective image fields thus obtained from the particular DD subproblem.

3.2. Constitutive rules for dislocations

The evolution of the dislocation structure is governed by the fields of the complete solution, i.e. the superposition of the DD sub-problems and the complete FE-elasticity solution. The Peach-Koehler force acting on dislocation I is thus calculated as:

$$f_i^{(I)} = n_i^{(I)} \left[\hat{\sigma}_{ij} + \sum_{J \neq I} \tilde{\sigma}_{ij}^{(J)} + \sigma_{ij}^{FE} \right] b_j^{(I)} \tag{4}$$

where $n^{(I)}$ is the normal to the slip plane containing the dislocation and $b^{(I)}$ is the dislocation Burgers vector, with the ($\tilde{}$) and ($\hat{}$) field solutions being used for the DD subproblem in which the dislocation lies. A linear mobility law with zero Peierls barrier is then used to calculate the dislocation glide velocity $\boldsymbol{v}^{(I)}$ as follows:

$$\boldsymbol{v}^{(I)} = \boldsymbol{f}^{(I)}/B \tag{5}$$

where B is the drag coefficient. The specimen is initially considered to be stress and dislocation free. Point sources, acting as a 2D representation of Frank-Read sources, are randomly dispersed with a density ρ_s throughout the niobium interlayer on slip planes spaced $d_{plane} = 200b$ apart unless otherwise stated. The sapphire is assumed to be purely linear-elastic at the loads and temperature considered; therefore, no sources are placed in the sapphire regions. Each source is prescribed a nucleation strength τ_{nuc} from a Gaussian distribution with mean $\bar{\tau}_{nuc}$ and a standard deviation of $0.2 \times \bar{\tau}_{nuc}$ for all three slip systems, as any anisotropy between slip systems and non-Schmid behaviour is disregarded in the model. Dislocation dipoles are nucleated if the resolved shear stress on the source is greater than τ_{nuc} for the duration of the nucleation time $t_{nuc} = 10$ ns. The sign of the dipole is determined by the direction of the resolved shear stress on the source. The dipole is generated with a spacing, L_{nuc}, given as:

$$L_{nuc} = \frac{\mu b}{2\pi(1-\nu)\tau_{nuc}} \tag{6}$$

where μ is the shear modulus, ν the Poisson's ratio and b the Burgers vector, such that the resolved shear stress exerted by one dislocation of the dipole on the other is balanced by τ_{nuc} so the dipole does not collapse.

Dislocations of opposite Burgers vector are annihilated when their spacing is less than or equal to $L_{ann} = 6b$ and a dislocation velocity cut-off is set at $v_{max} = 20$ m s^{-1}. Initial simulations showed that point obstacles to dislocation motion, as commonly included in planar dislocation dynamics simulations to represent dislocation junctions, small inclusions or precipitates, did not influence the mechanical response appreciably, since the high local stresses caused by confinement led to obstacles being easily overcome unless the obstacle strength was unrealistically high. Therefore, we do not include point obstacles to dislocation glide; only the layer interfaces block dislocations. These interfaces are taken to be perfectly impenetrable but dislocations are allowed to escape at the free surfaces.

3.3. DDP applied to current geometry

The specimen geometry is as shown in Fig. 3. We assume that the sapphire is completely linear elastic with shear modulus μ_{Sp} and Poisson's ratio υ_{Sp} and plasticity only occurs in the niobium interlayer with shear modulus μ_{Nb} and Poisson's ratio υ_{Nb}. Small strain conditions and material isotropy are assumed.

Plasticity in BCC materials such as niobium has a characteristic pencil glide appearance due to repeated cross-slip of screw dislocations [17]. When observing deformation for single crystal BCC micropillars, this leads to a uniform deformation along the pillar axis [20]. However, it has been observed that close to or above the critical temperature T_C of a BCC material, defined slip planes are observed and the behaviour approaches that of FCC metals [20, 21, 22]. Niobium has a $T_C = 290$ K [23] and the experiments in this study are performed at room temperature. Therefore, in the model we assume that slip occurs along defined slip planes without cross-slip. For BCC crystals, slip is known to occur in the closest packed <111> direction but on a number of slip planes, predominantly {110}, {112} and {123}. From Rice (1987) [24], when viewed in the $(10\bar{1})$ plane, plane-strain plastic deformation for a BCC crystal can arise on the (121) plane in the $[1\bar{1}1]$ direction, the $(\bar{1}2\bar{1})$ plane in the [111] direction and the (101) plane with simultaneous and equal slip in the $[\bar{1}\bar{1}1]$ and $[1\bar{1}\bar{1}]$ directions to give an effective, composite slip in the $[0\bar{1}0]$ direction. The niobium-sapphire relative orientation for the experiments is Nb(111)||Al_2O_3(0001) and accordingly the slip planes and directions used in the model satisfying plain strain conditions from Rice's analysis are oriented at $\phi_{i=1,2,3}$ =19.4°, 90° and 144.7° to the Nb-Al_2O_3 interface as shown in Fig. 3(a).

Screw dislocations have out-of-plane displacement and stress components and, therefore, cannot be modelled in plane strain DD simulations. For body-centred cubic materials below T_C, plasticity tends to be governed by the mobility of screw dislocations [17, 23, 25]. The $1/2 < 111 >$ screw dislocation splits into a

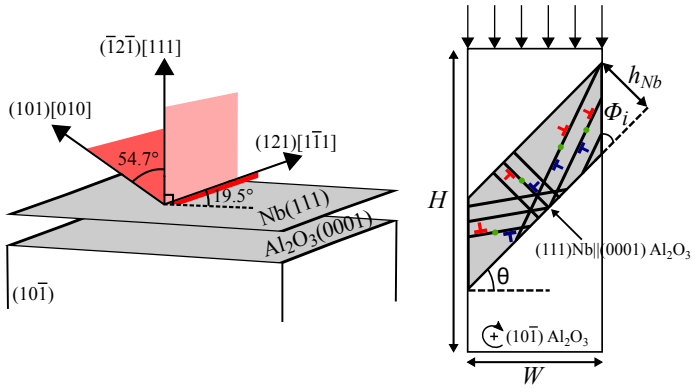


Figure 3: (a) Nb-Al_2O_3 bonding orientations with plane strain slip planes and directions shown for niobium. (b) Model geometry containing three slip systems.

non-planar core structure, leading to a higher Peierls potential that has to be overcome by thermal activation [25]. At low temperatures, these screw components have lower mobilities than non-screw components and, consequently, slip occurs through the motion of non-screw components. This is mostly achieved by the formation and then glide of kink-pairs, whose nucleation is a thermally activated process [17]. However, above the critical temperature T_C, the Peierls barrier for screw components is overcome by thermal activation alone and the mobility of screw dislocations becomes comparable to that of edge dislocations and the material response is similar to that of FCC metals [20, 22]. Therefore, close to or above Tc, plasticity is dominated by dislocation nucleation and glide with edge mobilities rather than other mechanisms such as kink-pair nucleation. As previously mentioned, the experiments are performed close to T_C of niobium, therefore allowing the use of a conventional DDP dislocation nucleation and glide model to study the mechanism involved, with the exact dislocation type that acts as the carrier of plasticity being of secondary importance.

The drag coefficient is chosen to be $B = 2\times10^{-4}$ Pa/s, the same as the drag coefficient of edge dislocations in BCC Fe [26] and Mo [27] at 293 K due to a lack of data for Nb in the literature. Loading is applied at a strain rate of $\dot{\varepsilon} = 2000\,\mathrm{s}^{-1}$ for compression of the top surface with a time step of $\Delta t = 0.5$ ns between increments, as in prior DDP studies [7, 9]. It has been shown that $\dot{\varepsilon} = 2000\,\mathrm{s}^{-1}$ lies within the rate independent regime for glide-only DDP [28] such that the simulation results and lower strain rate experiments can be suitably compared. A pillar height $H = 9\,\mu\mathrm{m}$ and width $W = 2.5\,\mu\mathrm{m}$ are fixed for all simulations, the same as the experiments. The Nb interlayer orientation is fixed at $\theta = 45°$ from the horizontal and thickness $h_{Nb} = 0.3\,\mu\mathrm{m}$ for all experiments and simulations, unless otherwise stated. For the finite element solutions, a conforming mesh consisting of a total of 1450 bi-linear, trapezoid shaped elements was constructed and convergent results obtained with a vertical node spacing of 0.1 µm for both materials and horizontal node spacing of 0.167 µm for the elastic sapphire and 0.071 µm for the plastic interlayer. A wider horizontal node spacing was assigned for the sapphire to save on computational costs. For the material interface, any node lying on both the boundary S_b and traction surface S_T was considered as part of S_b and disregarded from S_T for the O'Day implementation. When calculating the nodal forces caused by the tilda fields of dislocations, numerical integration is usually performed. However, proceeding with the ideas of Queyreau et al. (2014) [29] for 3DD and Tarleton et al. (2017) [30] for 2DD, the analytical solution of the force on a node due to a dislocation is used for higher accuracy and computational efficiency.

4. Results and discussion

4.1. Comparison with experiments

Different yield strengths for macroscopic niobium single crystals are reported in the literature [31, 32]. In discrete dislocation simulations, the sample yield strength is predominantly determined by the mean nucleation strength. As we shall see later, in simulating the experimental data in our case, a reasonable selection of the mean nucleation strength using the existing experimental literature does not affect the results and discussion significantly. Therefore, for our purposes, we assign $\bar{\tau}_{nuc}$ for our model to be 13 MPa, which is the critical resolved shear stress of the {110} and {112} slip systems determined by a previous crystal plasticity study for single crystal niobium [33]. However, for a source with $\tau_{nuc} = 13$ MPa, the nucleation dipole distance is $L_{nuc} = 0.129\,\mu\mathrm{m}$, which is comparable to the interlayer thickness $h_{Nb} = 0.3\,\mu\mathrm{m}$. If, for a particular source, $L_{nuc}/2$ is greater than the distance of the source to the interface, the newly nucleated dislocation is placed at the interface. In that case, two effects can occur: the dipole can collapse or the back stress can switch off the source until higher stresses are achieved.

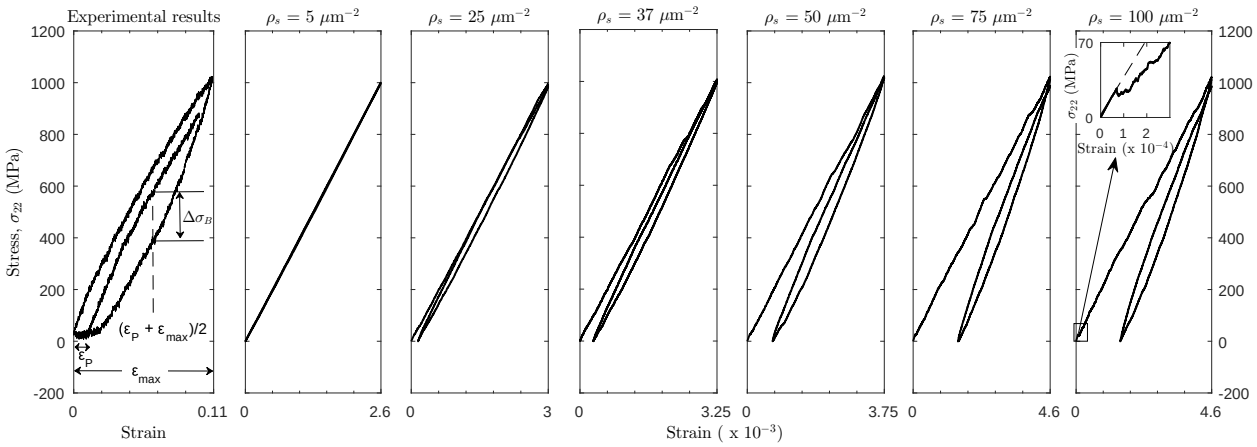


Figure 4: Experimental results and simulation stress-strain curves for $\bar{\tau}_{nuc} = 13$ MPa and different source densities. Note the strain axis has a different scale for each curve. The maximum strain during loading ε_{max}, the plastic strain upon unloading ε_p and the height of the hysteresis loop $\triangle\sigma_B$ are illustrated on the experimental results. The inset for $\rho_s = 100\,\mu m^{-2}$ shows the zoomed-in stress strain curve at the onset of yielding, the solid line representing the material response and the dashed line the perfectly elastic response.

μ_{Nb} (GPa)	ν_{Nb}	μ_{Sp} (GPa)	ν_{Sp}	b (nm)	B (Pa s)
47.2 [37]	0.36 [38]	183.2 [38]	0.16 [38]	0.286	2×10^{-4} [26, 27]

Table 1: Material parameters used in DDP simulations.

The experimental results and corresponding DDP simulation stress-strain curves for $\bar{\tau}_{nuc} = 13$ MPa and different source densities are shown in Fig. 4. The material parameters used are listed in Table 1. A conspicuous plastic hysteresis can be observed in both the experiment and simulations. It should be noted that the simulations have larger hardening rates than the experiment as indicated by the different strain axis scale. This has also been observed by other authors previously [12, 34] and is most commonly attributed to the effect of substrate and rig compliance making the overall experimental response less stiff [35, 36] without influencing the mechanism of deformation in the region of interest. In the case of the encapsulated-film micropillar geometry considered here, the difference can also be caused by the experimental samples being less confined than assumed in the model with a larger free surface to interface area from which dislocation escape can occur.

Simulations are run for different source densities ρ_s ranging from $5\,\mu m^{-2}$ to $100\,\mu m^{-2}$ to achieve the same maximum stress as the experiment and then unloaded to zero macroscopic stress and reloaded as seen in Fig. 4. The maximum strain recorded during loading is ε_{max} and the plastic strain upon unloading ε_p. The plastic proportion of the total loading is defined as $Q_P = \varepsilon_p/\varepsilon_{max}$ and the height of the hysteresis loop $\Delta\sigma_B$ is measured at $(\varepsilon_p + \varepsilon_{max})/2$. Q_P and $\Delta\sigma_B$ are then used to compare the simulation and experimental results.

In the simulations, both Q_P and $\Delta\sigma_B$ increase with increasing source density until saturation occurs at $\rho_s = 75\,\mu m^{-2}$ for the plastic proportion Q_P and $\rho_s = 50\,\mu m^{-2}$ for the hysteresis loop $\Delta\sigma_B$. The size of the hysteresis loop $\Delta\sigma_B$ for the experiment is approximately 2 times larger than the maximum $\Delta\sigma_B$ for the simulations. It should be noted that the experiments demonstrate a parabolic hardening response, whereas the conventional DDP results give linear hardening which can be attributed to a static source structure and lack of more complex dislocation interactions. Incorporating cross-slip, junction formation and a dynamic

source structure in the simulations as in the so-called 2.5DD [39], parabolic loading and unloading curves would be observed giving a larger $\Delta\sigma_B$. It is found that $\rho_s = 50\,\mu\text{m}^{-2}$, with the maximum $\Delta\sigma_B$ out of the densities considered and $Q_P = 0.18$, matches the experimental results for which $Q_P \sim 0.17$.

In previous simultaneous experimental and DD studies for small-scale plasticity, experimental samples were found to be in the source-limited regime [7, 40]. For the case of the BCC thin films considered here, we establish that the experimental samples correspond to the saturated source density regime with the maximum Bauschinger effect; thus, the samples are not source limited. Physically, this can be attributed to the highly confined, small volume of the Nb film which has limited dislocation escape and a large amount of dislocation interactions leading to a large number of sources being formed.

The onset of plasticity in the experimental stress-strain curve is not easily distinguishable whereas a clear transition can be seen in the zoomed-in section of the simulation results as shown for $\rho_s = 100\,\mu\text{m}^{-2}$. Due to the low yield strength and, hence, mean nucleation strength of niobium, flow occurs at a relatively low stress compared to the maximum stress achieved and the majority of the specimen response is post-yielding. Moreover, the highly confined film dimensions lead to a strong hardening effect. A higher $\bar{\tau}_{nuc}$ value, e.g. 50 MPa, also motivated from the existing single crystal niobium experimental literature [32], leads to yield occurring at a slightly larger stress but overall the results remain similar. Therefore, as stated previously, the choice of $\bar{\tau}_{nuc}$ does not affect the results significantly in this case. Indeed, the indistinguishable yielding in the experimental data provides further justification for the lower $\bar{\tau}_{nuc}$ used here.

The dislocation structure and stress state for the representative $\bar{\tau}_{nuc} = 13$ MPa and $\rho_s = 50\ \mu\text{m}^{-2}$ at maximum loading and unloading are shown in Fig. 5. Upon loading, both primary and secondary slip activation is observed and dislocation pile-ups occur at the impenetrable interface. These pile-ups cause a highly heterogeneous stress state in the niobium film, with regions under significant tensile stresses even being visible in the stress map in Fig. 5(a) (tensile stresses are shown as negative, see on-line version for coloured annotation). These tensile stressed regions can become nucleation points for micro-cracks. Fig. 5(b) shows the stress state and dislocation structure upon unloading to zero macroscopic stress. The pile-ups relax, although a significant dislocation density remains since only a few slip planes terminate at the free surface and dislocation escape is limited. This residual dislocation density contributes to the plastic strain observed in Fig. 4.

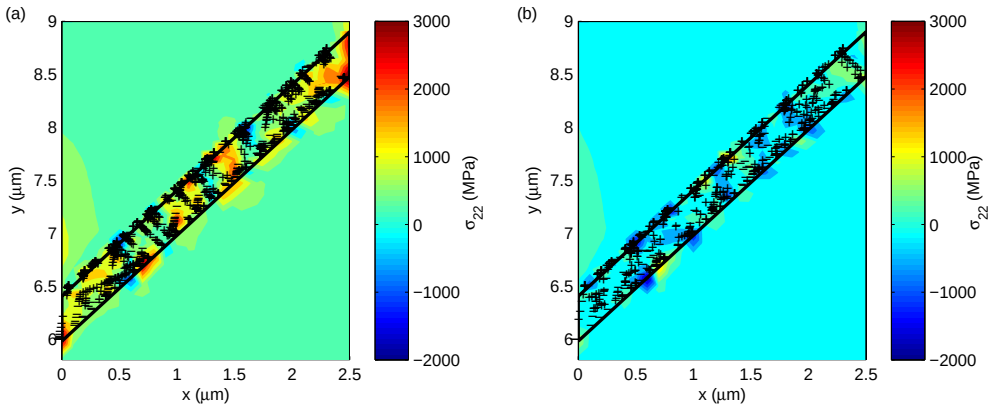


Figure 5: Compressive stress σ_{22} state and dislocation structure for the $\bar{\tau}_{nuc} = 13$ MPa and $\rho_s = 50\,\mu\text{m}^{-2}$ sample at (a) maximum loading and (b) unloading to zero macroscopic stress. Compressive stresses are shown positive.

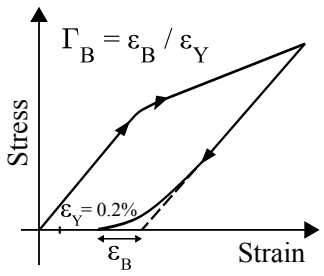


Figure 6: Measure of the Bauschinger effect in small-scale samples.

4.2. Effect of source density and mean nucleation strength

The effect of source density ρ_s and mean nucleation strength $\bar{\tau}_{nuc}$ on the yield strength and hardening rate have been analysed in the literature previously [41, 42]. Briefly, a higher source density leads to an increased likelihood of a lower strength source, giving rise to a lower yield strength and a greater number of sources that can nucleate at a given applied stress, resulting in a lower hardening rate. There is an increase in the yield strength with increasing $\bar{\tau}_{nuc}$ but little effect on the hardening rate once yielding has occurred. Here, the effect of source density and nucleation strength on reverse plasticity is analysed in detail.

In the previous section, all simulations were performed to different strains in order to achieve the same stress levels as the experiments. In order to understand the effect of mean nucleation strength and source density on the Bauschinger effect quantitatively, we now perform simulations to a total maximum strain of $\varepsilon_{max} = 0.5\%$ and analyse the trends. The mean nucleation strength $\bar{\tau}_{nuc}$ is varied from 13 to 100 MPa and the source density ρ_s from 5 to 200 μm^{-2}. Disregarding changes in the mechanism of plastic flow, changes in the test temperature and sample preparation conditions can be represented by a different mean nucleation strength and source density respectively. Two source placement strategies are considered. First, the slip plane spacing d_{plane} is fixed at $200b$, a slip plane chosen arbitrarily and a source randomly placed along it; no restriction is made on the number of sources on each plane. The second source placement involves placing only one source per plane with the slip plane spacing being varied to achieve different source densities such that $d_{\text{plane}} \propto 1/\rho_s$ for fixed film dimensions. At least three repeats were performed for each source density and mean nucleation strength, and the Bauschinger effect Γ_B measured as shown in Fig. 6. A two term exponential curve was then fit to the mean Γ_B values. The results for the entire parameter range for both the random source placement and one source per plane are shown in Fig. 7.

For the random source placement, considering the effect of source density at $\bar{\tau}_{nuc} = 13$ MPa, the Bauschinger effect increases sharply and then decreases with increasing source densities, the maximum

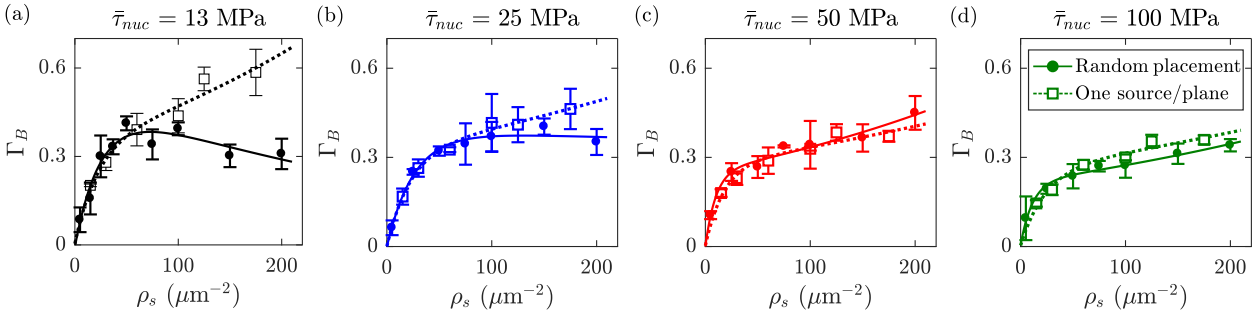
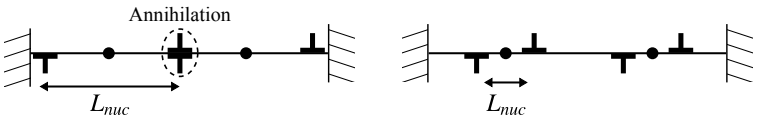


Figure 7: The mean Bauschinger effect $\bar{\Gamma}_B$ against ρ_s for $\bar{\tau}_{nuc}$ of (a) 13 MPa, (b) 25 MPa, (c) 50 MPa and (d) 100 MPa.



(a) Low $\bar{\tau}_{nuc}$. (b) High $\bar{\tau}_{nuc}$.

Figure 8: High ρ_s case with two sources on the same slip plane. (a) Low $\bar{\tau}_{nuc}$ sources with large L_{nuc} leading to immediate annihilation. (b) High $\bar{\tau}_{nuc}$ sources with small L_{nuc}.

occurring at around $\rho_s = 70\ \mu\text{m}^{-2}$. As $\bar{\tau}_{nuc}$ is increased, however, this maximum shifts to a higher source density, such that for $\bar{\tau}_{nuc} = 50$ or 100 MPa, for the source densities considered, the Bauschinger effect only increases with increasing source density. On the other hand, for the case of only one source per plane, the Bauschinger effect increases monotonically with source density for all nucleation strengths. A rationale for this observation is as follows.

At low source densities, when no more than one source occurs per slip plane for either source placement strategies, increasing the source density increases the number of pile-ups in the specimen and, thus, the Bauschinger effect assuming that each source gives rise to two pile-ups at the opposing interfaces. For random source placement, there is an increased likelihood of two or more sources occurring on the same slip plane as the source density is increased. For such situations, dislocations nucleated into the region between the sources have opposite Burgers vector as illustrated in Fig. 8. Assuming a homogeneous stress state in the film, the two sources will activate at the same rate. At lower $\bar{\tau}_{nuc}$, the nucleation distance L_{nuc} is large enough such that the dislocations nucleated on the same plane can immediately interact and annihilate. In this instance, on average, there will be less than two pile-ups per source. For a higher $\bar{\tau}_{nuc}$ where there is a smaller L_{nuc}, this is not the case. The newly nucleated dislocations are still some distance apart and do not annihilate. Rather, due to interaction with dislocations on other planes (latent hardening), these dislocations may become confined to form a non-interfacial pile-up with the average number of pile-ups per source again approaching two. Whereas, with the restriction of one source per plane, the number of pile ups per source remains at two and there is only an increase in the number of pile-ups and the Bauschinger effect with increasing source density regardless of the nucleation strength and dipole spacing.

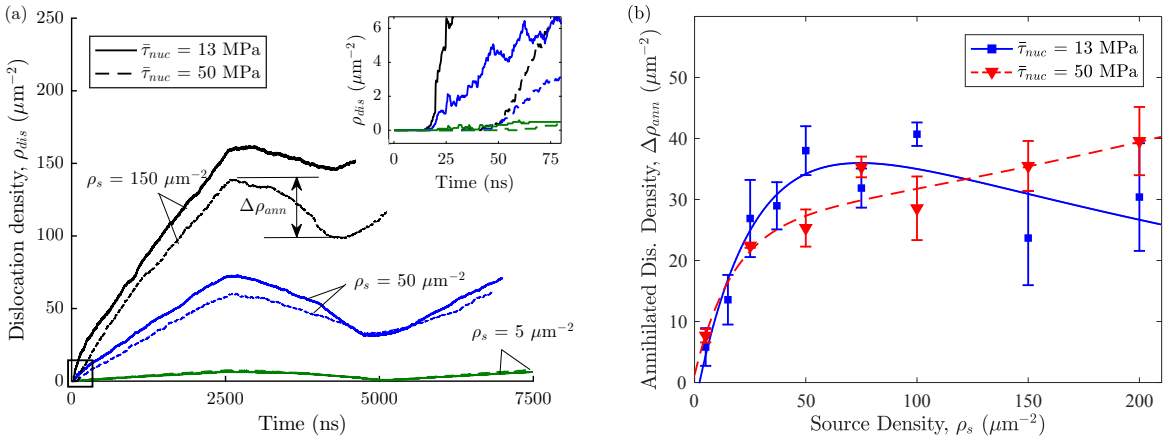


Figure 9: (a) Dislocation density ρ_{dis} evolution against time during simulations for $\bar{\tau}_{nuc} = 13$ and 50 MPa for random source placement with source densities $\rho_s = 5$, 50 and 150 μm^{-2}. The measurement of the annihilated dislocation density $\triangle\rho_{ann}$ is also shown. The inset shows a zoomed-in view of the onset of plasticity. (b) The annihilated dislocation density $\triangle\rho_{ann}$ against source density for $\bar{\tau}_{nuc} = 13$ and 50 MPa.

The discussion above suggests that the number of dislocations that annihilate on unloading can give a measure of the number of pile-ups and dislocations available for reverse glide to begin with and, hence, is related to the size of the Bauschinger effect. These dislocations are represented by the decrease in the dislocation density when unloading occurs. It is important to note that the dislocation density ρ_{dis} is calculated as the number of dislocations in the sample divided by the total area of the entire specimen, since the macroscopic stress of the combined elastic-plastic system/micropillar is being observed in our case. Fig. 9(a) shows the evolution of ρ_{dis} with loading increments for selected source densities for $\bar{\tau}_{nuc} = 13$ MPa and $\bar{\tau}_{nuc} = 50$ MPa using the random source placement strategy. Higher dislocation densities are built up with increased source densities for each $\bar{\tau}_{nuc}$, but for a particular source density, a higher dislocation density occurs for the lower $\bar{\tau}_{nuc}$ due to an earlier initiation of plasticity. This can be observed in the inset in Fig. 9(a), where the dislocation density begins to increase at a smaller strain for $\bar{\tau}_{nuc} = 13$ MPa than $\bar{\tau}_{nuc} = 50$ MPa and then the rate of increase of ρ_{dis} is the same for both $\bar{\tau}_{nuc}$. The small decrease in the Bauschinger effect observed in Fig. 7 at the transition source density with increasing $\bar{\tau}_{nuc}$ is attributed to these different plastic pre-strains.

The decrease in dislocation density $\Delta\rho_{ann}$, as shown on Fig. 9(a), caused by annihilation on reverse loading is measured and plotted for $\bar{\tau}_{nuc} = 13$ MPa and 50 MPa in Fig. 9(b) for all source densities considered with a random source placement. As the source density is increased beyond the point where more than two sources are likely to exist on the same plane, $\Delta\rho_{ann}$ decreases for the lower mean nucleation strength $\bar{\tau}_{nuc} = 13$ MPa, whereas for $\bar{\tau}_{nuc} = 50$ MPa, it continues to increase. Importantly, a similar trend to the size of the Bauschinger effect in Fig. 7(a) and (c) is observed, suggesting a link between plastic hysteresis and the annihilated dislocation density. To elaborate on this relationship more clearly, we plot the size of the Bauschinger effect Γ_B against $\Delta\rho_{ann}$ for all simulations performed for the different ρ_s and $\bar{\tau}_{nuc}$ in Fig. 10(a) for both types of source placement. A clear linear trend can be seen, suggesting that the annihilated dislocation density is a good representation of the number of dislocations that undergo reverse glide in such samples. This supports our previous discussion that the source density and mean nucleation strength have a coupled effect on the number of dislocations available for reverse glide which in turn determines the size of the Bauschinger effect.

Conventionally, the size of the Bauschinger effect has been linked to the amount of plastic prestrain before

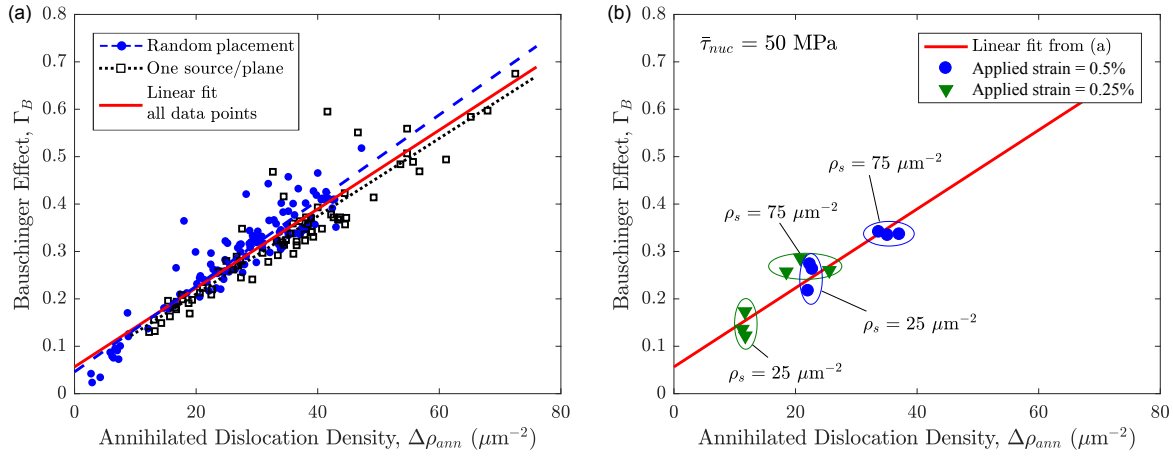


Figure 10: Plot of Bauschinger effect Γ_B against annihilated dislocation density $\triangle\rho_{ann}$ for all ρ_s and $\bar{\tau}_{nuc}$ for a film with $h_{Nb} = 0.3\,\mu$m and $\theta = 45°$.

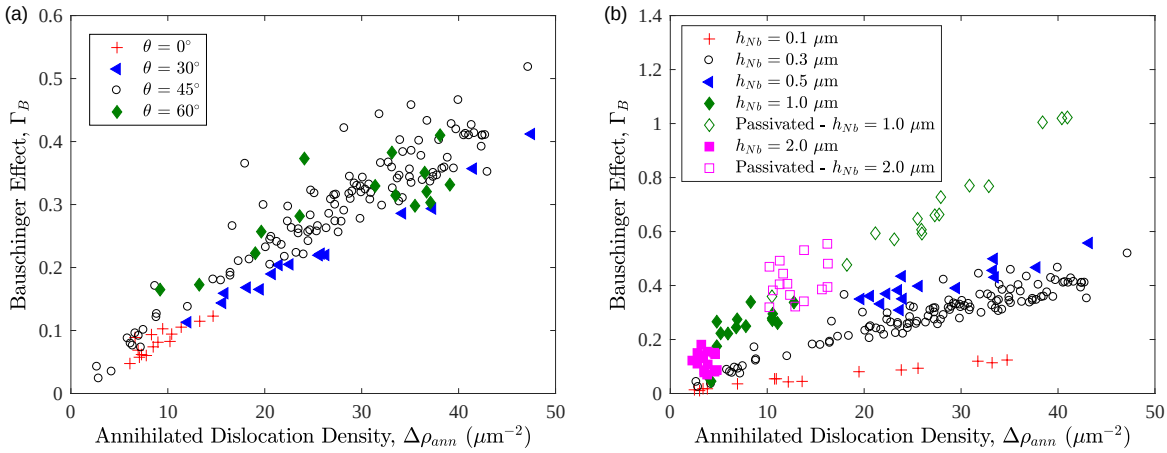


Figure 11: Bauschinger effect Γ_B against annihilated dislocation density $\triangle\rho_{ann}$ for (a) different film orientations θ for a 0.3 µm film thickness and (b) different film thicknesses h_{Nb} for a 45° film orientation.

unloading [7, 9]. In the previous discussion, samples were naturally loaded to different plastic prestrains despite the same total applied strain due to the variation in sample nucleation strength leading to different yield strains. However, to explicitly show the effect of plastic prestrain, we perform simulations for a fixed nucleation strength for total applied strains of 0.5% and 0.25%. The results are shown in Fig. 10(b) for two source densities together with the linear Γ_B vs. $\Delta\rho_{ann}$ relationship obtained previously. The larger prestrain leads to more dislocations being stored in pile-ups and thus a larger Bauschinger effect. Importantly, the annihilated dislocation density can again be used to account for the effect of plastic prestrain. Thus the linear Γ_B against $\Delta\rho_{ann}$ relationship holds for different plastic prestrains as well.

4.3. Orientation and size effect

Lastly, we investigate geometric effects on the extent of reverse plasticity. For a 0.3 µm film thickness, Nb film orientations of $\theta = 0°$, 30° and 60° to the horizontal are considered and compared to the 45° orientation results from the previous section. For each orientation, different source densities for $\bar{\tau}_{nuc} = 50$ MPa are simulated to achieve a range of sizes of the Bauschinger effect. Random source placement is used since it is physically more relevant. It should be noted that the niobium and sapphire crystal orientations are maintained at Nb(111)||Al_2O_3(0001) implying that changing the film angle not only changes the relative volumes and geometry of niobium to sapphire, but also the niobium crystal orientation with regard to the axis of loading. Next, fixing the film orientation at 45°, thicknesses of $h_{Nb} = 0.1$µm, 0.5µm, 1.0µm and 2.0µm are also simulated at $\bar{\tau}_{nuc} = 50$ MPa and different source densities, and compared to the 0.3 µm film from the previous section. As the film thickness increases, the mechanical response becomes gradually less stiff as the relative volume of Nb increases in the specimen and there is less hardening because of an increasing proportion of free surfaces for dislocations to escape from. The mechanical response of the micropillars obtained is thus different as either the orientation or film thickness is varied.

Fig. 11(a) and (b) plot Γ_B against annihilated dislocation density $\Delta\rho_{ann}$ for the different film orientations and thicknesses respectively. It is important to note here that the Bauschinger effect varies with both changing film orientation and thickness, e.g. Fig. 11(a) shows that the $\theta = 0°$ film has, on average, a smaller Γ_B compared to other orientations. This is because there is a smaller volume of niobium in the specimen when the orientation angle is smaller, and less slip activation due to an unfavourable crystal orientation in the $\theta = 0°$ case. However, if we use the annihilated dislocation density to correlate with Γ_B, the same linear

trend is obtained for the Bauschinger effect against $\Delta\rho_{ann}$ for all film orientations. The effect of changing the film thickness, on the other hand, leads to the formation of bands with different slopes for each thickness as shown in Fig. 11(b). This suggests that the Bauschinger effect also has a length-scale dependence in addition to the annihilated dislocation density.

Results are also plotted for films completely passivated from the left and right sides for the 1.0 µm and 2.0 µm film thicknesses, but assuming zero passivation thickness. Where dislocations could escape from the free surfaces, pile-ups now occur at the passivated sides in addition to the niobium-sapphire interface. Reverse glide from these pile-ups can again be represented by the annihilated dislocation density upon unloading. Thus, the passivated and unpassivated specimens appear to lie on the same linear plot, but with the passivated films just having a larger Bauschinger effect as seen in 11(b).

4.4. Measure of reverse glide as a unifying concept

Fig. 11(b) indicates that in addition to a measure of the number of dislocations that undergo reverse glide per unit volume, the Bauschinger effect also has a length scale dependence. We postulate that this length scale would represent the distance over which reverse glide occurs, i.e. the mean free path for dislocations and suggest a relationship of the form:

$$\Gamma_B = \Gamma_o + \beta\Delta\rho_{ann}(l/l_0)^n \tag{7}$$

where Γ_o represents reverse plasticity caused by the dislocation density that undergoes reverse glide but does not annihilate, l is the mean free path for dislocations and n is an exponent to be determined. In Eq. 7, we define l_0 as a reference length scale fixed here at 1.0 µm such that β is a constant coefficient with dimensions µm^2 for all values of the exponent n. Using the film thickness h_{Nb} as a measure of the mean free path for dislocations, the best fit equation for all data for different film thicknesses is shown in Fig. 12. The exponent n is found to be 0.65. A good agreement with the data is obtained with an adjusted R-squared value of 0.9033. We also investigate the effect of considering data points for additional film thicknesses of $h_{Nb} = 0.2$ µm and 0.75 µm on the best fit plot. Table 2 shows the effect of including an increased number of film thicknesses sequentially in the analysis on the value of n and the adjusted R-squared value of the best fit. It can be seen that n converges to a value close to 0.65-0.67 with an adjusted R-squared value remaining above 0.9, demonstrating a good fit. Thus, we propose the use of $\Delta\rho_{ann} \times (l/l_0)^n$ as a measure of the amount of net reverse glide that occurs in the confined specimen that accounts for dependence of nucleation strength, source density, plastic prestrain, crystal orientation and film thickness on the Bauschinger effect. For our simulations, a value of $n = 0.65$ demonstrates a good fit. We postulate that $\Delta\rho_{ann}$ represents the density of dislocations that undergo reverse glide in a confined volume, l the distance over which reverse glide occurs and n constitutes a measure of dislocation interaction affecting the mean free path, e.g. self-hardening induced by pile-ups, or latent hardening.

Recently, suggestions have been made to incorporate micro-mechanically based dislocation interaction terms into previously phenomenological expressions of size dependence of yield strengths such as the Hall-Petch effect. Gu and Ngan (2013) [43] developed a theoretical model assuming that yield strengths are determined by Taylor interactions between dislocations and showed that the size effect arises as a consequence of a power-law distribution of free dislocation segments. El-Awady (2015) [44] developed a generalised model incorporating grain sizes and initial dislocation densities to predict size effects over a range of scales and also showed that the Hall-Petch effect in polycrystals can be recovered from the derived model by assuming a particular kinematic dislocation density evolution. Other models have used statistical arguments to derive

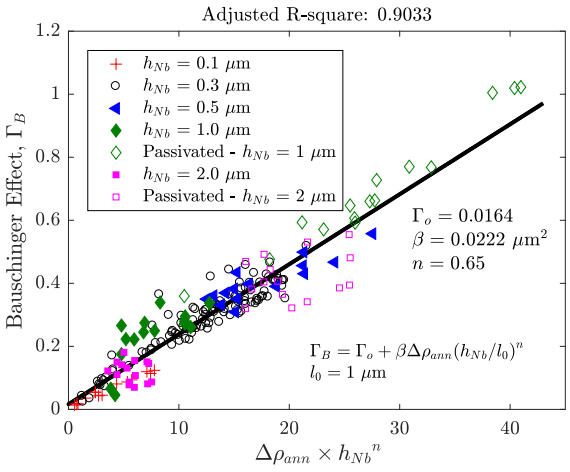


Figure 12: Γ_B against $\triangle\rho_{ann} \times {h_{Nb}}^n$ for different film thicknesses, with $n = 0.65$ found to give the best fit equation.

No. of film thicknesses considered	3	4	5	6	7
n value	0.65	0.65	0.65	0.66	0.67
Adjusted R-squared value	0.8925	0.9057	0.9033	0.9045	0.9011

Table 2: Convergence of best fit plot as sequential film thicknesses are added to analysis.

the stress required to activate sources at a given crystal size and dislocation density [45, 46]. Since these models are concerned with predicting first yield, there is an element of accounting for dislocation nucleation and evolution, and less discussion of glide areas. Whereas our approach here is concerned with relating the motion of dislocations to the extent of plasticity, or to be precise in our case, reverse plasticity. Nevertheless, our results support looking at reverse plasticity as well in the context of length scales and dislocation densities which to date has not been established. Further work is being done to investigate the physical basis for n, the length-scale exponent and to determine if a similar relationship applies to less confined geometries and to climb-activated dislocation motion.

5. Conclusions

Plane strain discrete dislocation simulations have been used to interpret the experimental observation of the Bauschinger effect in an encapsulated-thin film micropillar system. The O'Day method was implemented to account for the different elastic properties of the thin niobium film and the sapphire substrate in the micropillar. The following conclusions can be drawn from the analysis:

1. The experimental samples correspond to a saturated source density regime with the maximum Bauschinger effect for the chosen mean nucleation strength. This is attributed to the large amount of dislocation interactions that occur in the highly confined small volume resulting in a large number of sources.
2. The effect of source density and mean nucleation strength on the Bauschinger effect is analysed in detail. It is found that there is a coupled source density and mean nucleation strength effect on the size of plastic hysteresis. For random source placement and low $\bar{\tau}_{nuc}$, the Bauschinger effect increases to a maximum then decreases with increasing source density whereas for high $\bar{\tau}_{nuc}$, the Bauschinger effect continues to increase for the considered source densities. When source structures with only one source per plane are considered, the Bauschinger effect increases monotonically with increasing source density for all nucleation strengths.

3. This effect is linked to the difference in the number of pile-ups per source and the consequent dislocations available for reverse glide. For low $\bar{\tau}_{nuc}$, the nucleation distance is large such that dislocations nucleated from two sources lying on the same plane annihilate immediately. For a high $\bar{\tau}_{nuc}$, these dislocations are nucleated at a distance because of the lower L_{nuc} and can thus cause a pile-up without an interface and be available for reverse glide on unloading.
4. For all source densities and nucleation strengths considered for a particular sample size, it is shown that there is a linear relationship between the density of dislocations annihilated on unloading $\Delta\rho_{ann}$ and the size of the Bauschinger effect. This supports the discussion that source density and nucleation strength have a coupled effect on the number of pile-ups that form from which reverse glide and annihilation can occur.
5. Changing the film orientation has no effect on this linear relationship whereas for different film thicknesses, bands with different slopes are obtained on the Γ_B versus $\Delta\rho_{ann}$ graph, implying a length scale dependence on the size of the Bauschinger effect.
6. A unifying relationship of the form $\Gamma_B = \Gamma_o + \beta\Delta\rho_{ann}(l/l_0)^n$ with an exponent of $n = 0.65$ is found to fit the data points for different thicknesses, source densities and mean nucleation strengths considered here. It is suggested that $\Delta\rho_{ann} \times (l/l_0)^n$ represents a measure of the net reverse dislocation glide that occurs in the specimen and thus provides a linear relationship with the Bauschinger effect. In particular, we postulate that $\Delta\rho_{ann}$ represents the dislocations that undergo reverse glide and l is the distance over which reverse glide occurs, with the coefficient n representing the effect of different hardening mechanisms.

Acknowledgements

S. W acknowledges financial support from the Imperial College President's fund.

References

[1] Julia R. Greer and Jeff Th M De Hosson. Plasticity in small-sized metallic systems: Intrinsic versus extrinsic size effect. *Progress in Materials Science*, 56:654–724, 2011.

[2] Ray S. Fertig and Shefford P. Baker. Simulation of dislocations and strength in thin films: A review. *Progress in Materials Science*, 54:874–908, 2009.

[3] R.P. Vinci, E.M. Zielinski, and J.C. Bravman. Thermal strain and stress in copper thin films. *Thin Solid Films*, 262(1-2):142–153, 1995.

[4] Y. Xiang and J. J. Vlassak. Bauschinger and size effects in thin-film plasticity. *Acta Materialia*, 54:5449–5460, 2006.

[5] Jong H Han and M Taher A Saif. In situ microtensile stage for electromechanical characterization of nanoscale freestanding films. *Review of Scientific Instruments*, 77:045102, 2006.

[6] A. T. Jennings, C. Gross, F. Greer, Z. H. Aitken, S. W. Lee, C. R. Weinberger, and J. R. Greer. Higher compressive strengths and the Bauschinger effect in conformally passivated copper nanopillars. *Acta Materialia*, 60:3444–3455, 2012.

[7] L. Nicola, Y. Xiang, J. J. Vlassak, E. Van der Giessen, and A. Needleman. Plastic deformation of freestanding thin films: Experiments and modeling. *Journal of the Mechanics and Physics of Solids*, 54(10):2089–2110, 2006.

[8] Jagannathan Rajagopalan, Jong H. Han, and M. Taher A. Saif. Bauschinger effect in unpassivated freestanding nanoscale metal films. *Scripta Materialia*, 59:734–737, 2008.

[9] S. Shishvan, L. Nicola, and E. Van Der Giessen. Bauschinger effect in unpassivated freestanding thin films. *Journal of Applied Physics*, 107(9):1–9, 2010.

[10] Caizhi Zhou and Richard Lesar. Dislocation dynamics simulations of the Bauschinger effect in metallic thin films. *Computational Materials Science*, 54(1):350–355, 2012.

[11] P. J. Guruprasad, W. J. Carter, and A. A. Benzerga. A discrete dislocation analysis of the Bauschinger effect in microcrystals. *Acta Materialia*, 56(19):5477–5491, 2008.

[12] Seok Woo Lee, Andrew T. Jennings, and Julia R. Greer. Emergence of enhanced strengths and Bauschinger effect in conformally passivated copper nanopillars as revealed by dislocation dynamics. *Acta Materialia*, 61(6):1872–1885, 2013.

[13] Yi Nan Cui, Zhan Li Liu, and Zhuo Zhuang. Theoretical and numerical investigations on confined plasticity in micropillars. *Journal of the Mechanics and Physics of Solids*, 76:127–143, 2015.

[14] Yang Mu, J W Hutchinson, and W J Meng. Micro-pillar measurements of plasticity in confined Cu thin films. *Extreme Mechanics Letters*, 1:62–69, 2014.

[15] Erik Van der Giessen and Alan Needleman. Discrete dislocation plasticity: a simple planar model. *Modelling and Simulation in Materials Science and Engineering*, 3:689–735, 1995.

[16] V A Lubarda, J A Blume, and A Needleman. An Analysis of Equilibrium Dislocation Distributions. *Acta Metallurgica et Materialia*, 41(2):625–642, 1993.

[17] John Price Hirth and Jens Lothe. Theory of Dislocations, second edition. *John Wiley and Sons, New York*, 1982.

[18] M. P. O'Day and William A. Curtin. A Superposition Framework for Discrete Dislocation Plasticity. *Journal of Applied Mechanics*, 71(6):805–815, 2004.

[19] Siamak Soleymani Shishvan, Soheil Mohammadi, Mohammad Rahimian, and Erik Van Der Giessen. Plane-strain discrete dislocation plasticity incorporating anisotropic elasticity. *International Journal of Solids and Structures*, 48(2):374–387, 2011.

[20] Ju Young Kim, Dongchan Jang, and Julia R. Greer. Tensile and compressive behavior of tungsten, molybdenum, tantalum and niobium at the nanoscale. *Acta Materialia*, 58:2355–2363, 2010.

[21] Ju Young Kim, Dongchan Jang, and Julia R. Greer. Insight into the deformation behavior of niobium single crystals under uniaxial compression and tension at the nanoscale. *Scripta Materialia*, 61:300–303, 2009.

[22] A. S. Schneider, D. Kaufmann, B. G. Clark, C. P. Frick, P. A. Gruber, R. Mönig, O. Kraft, and E. Arzt. Correlation between critical temperature and strength of small-scale bcc pillars. *Physical Review Letters*, 103:1–4, 2009.

[23] Takayoshi Suzuki, Hirokazu Koizumi, and Helmut O. K. Kirchner. Plastic flow stress of b.c.c. transition metals and the peierls potential. *Acta Metallurgica et Materialia*, 43(6):2177–2187, 1995.

[24] James R Rice. Tensile crack tip fields in elastic-ideally plastic crystals. *Mechanics of Materials*, 6:317–335, 1987.

[25] V Vitek. Core structure of screw dislocations in body-centred cubic metals: relation to symmetry and interatomic bonding. *Philosophical Magazine*, 84:415–428, 2004.

[26] S Queyreau, J Marian, M R Gilbert, and B D Wirth. Edge dislocation mobilities in bcc Fe obtained by molecular dynamics. *Physical Review B - Condensed Matter and Materials Physics*, 84:064106, 2011.

[27] Jinpeng Chang, Wei Cai, Vasily V Bulatov, and Sidney Yip. Dislocation motion in BCC metals by molecular dynamics. *Materials Science and Engineering A*, 309-310:160–163, 2001.

[28] Prabhat K. Agnihotri and Erik Van Der Giessen. On the rate sensitivity in discrete dislocation plasticity. *Mechanics of Materials*, 90:37–46, 2015.

[29] S Queyreau, J Marian, BD Wirth, and A Arsenlis. Analytical integration of the forces induced by dislocations on a surface element. *Modelling and Simulation in Materials Science and Engineering*, 22:035004, 2014.

[30] E Tarleton and D S Balint. A Discrete Dislocation Plasticity Study of the Ductile-Brittle Transition. *To be submitted for publication*, 2017.

[31] Thomas Gnäupel Herold, Ganapati Rao Myneni, and Richard E Ricker. Investigations of Residual Stresses and Mechanical Properties of Single Crystal Niobium for SRF Cavities. *AIP Conference Proceedings*, 48(927):48–59, 2007.

[32] Ganapati Rao Myneni. Physical and Mechanical Properties of Niobium for SRF Science and Technology. *AIP Conference Proceedings*, 41(927):41–47, 2007.

[33] A Siddiq and S Schmauder. Interface fracture analyses of a bicrystal niobium / alumina specimen using a cohesive modelling approach. *Modelling and Simulation in Materials Science and Engineering*, 14:1015–1030, 2006.

[34] Rodrigo A. Bernal, Amin Aghaei, Sangjun Lee, Seunghwa Ryu, Kwonnam Sohn, Jiaxing Huang, Wei Cai, and Horacio Espinosa. Intrinsic Bauschinger Effect and Recoverable Plasticity in Pentatwinned Silver Nanowires Tested in Tension. *Nano Letters*, 15:139–146, 2015.

[35] In-suk Choi, Yixiang Gan, Daniel Kaufmann, Oliver Kraft, and Ruth Schwaiger. Measurement of Young's modulus of anisotropic materials using microcompression testing. *Journal of Materials Research*, 27:2752–2759, 2012.

[36] Zhen Zhang, Tea Sung Jun, T. Benjamin Britton, and Fionn P E Dunne. Intrinsic anisotropy of strain rate sensitivity in single crystal alpha titanium. *Acta Materialia*, 118:317–330, 2016.

[37] M S Duesbery and V Vitek. Plastic anisotropy in B.C.C transition metals. *Acta Materialia*, 46(5):1481–1492, 1998.

[38] D Korn, G Elssner, R M Cannon, and M Ruhle. Fracture properties of interfacially doped Nb-Al2O3 bicrystals: I , fracture characteristics. *Acta Materialia*, 50:3881–3901, 2002.

[39] A A Benzerga, Y Brechet, A Needleman, and E Van Der Giessen. Incorporating three-dimensional mechanisms into two-dimensional dislocation dynamics. *Modelling and Simulation in Materials Science and Engineering*, 12(3):159–169, 2004.

[40] E Tarleton, D S Balint, J Gong, and A J Wilkinson. A discrete dislocation plasticity study of the micro-cantilever size effect. *Acta Materialia*, 88:271–282, 2015.

[41] D S Balint, V S Deshpande, and A Needleman. Discrete dislocation plasticity analysis of the grain size dependence of the flow strength of polycrystals. *International Journal of Plasticity*, 24:2149–2172, 2008.

[42] Srinath S. Chakravarthy and W. A. Curtin. Effect of source and obstacle strengths on yield stress: A discrete dislocation study. *Journal of the Mechanics and Physics of Solids*, 58(5):625–635, 2010.

[43] R. Gu and A. H W Ngan. Dislocation arrangement in small crystal volumes determines power-law size dependence of yield strength. *Journal of the Mechanics and Physics of Solids*, 61(6):1531–1542, 2013.

[44] Jaafar A El-Awady. Unravelling the physics of size-dependent dislocation-mediated plasticity. *Nature communications*, 6:5926, 2015.

[45] Triplicane A Parthasarathy, Satish I Rao, Dennis M Dimiduk, Michael D Uchic, and Dallas R Trinkle. Contribution to size effect of yield strength from the stochastics of dislocation source lengths in finite samples. *Scripta Materialia*, 56:313–316, 2007.

[46] Seok-Woo Lee and William D. Nix. Size dependence of the yield strength of fcc and bcc metallic micropillars with diameters of a few micrometers. *Philosophical Magazine*, 92(10):1238–1260, 2012.